Supplementary material for "Robust estimates of the ratio between S- and P-wave velocity anomalies in the Earth's mantle using normal modes"

Federica Restelli[1,†], Christophe Zaroli[2] & Paula Koelemeijer[1,3*]

[1] Department of Earth Sciences, Queen's Building. Royal Holloway University of London, Egham Hill, Egham, Surrey, TW20 0EX, United Kingdom
[2] Institut Terre et Environnement de Strasbourg, UMR 7063, Université de Strasbourg, EOST/CNRS, 67084 Strasbourg cedex, France.
[3] Department of Earth Sciences, University of Oxford, South Parks Road, Oxford, OX1 3AN UK, United Kingdom
† Corresponding author. Email: federica.restelli.2019@live.rhul.ac.uk
* Email: paula.koelemeijer@earth.ox.ac.uk

Contents:

Table S1 lists the 16 tomographic models used in the calculation of the 3D noise (as detailed in Section 3.4 in the main text). In some studies, v_p perturbations were directly inverted for, in other studies they were scaled from v_s perturbations (using particular $\mathrm{dln}v_p/\mathrm{dln}v_s$ scaling factors as indicated in the table). Density perturbations are always obtained by scaling them from v_s perturbations, with the $\mathrm{dln}\rho/\mathrm{dln}v_s$ scaling factor also given in the table.

Table S1: List of tomography models (in chronological order) used for the estimation of the 3D noise, including any scaling factors for v_p and density perturbations. We scale v_p and ρ according to the original studies, wherever this information is provided (bold values). If no information on the scaling was provided, we set $\mathrm{dln}v_p/\mathrm{dln}v_s$=0.5 and $\mathrm{dln}\rho/\mathrm{dln}v_s$=0.3.

Model	$\mathrm{dln}v_p/\mathrm{dln}v_s$	$\mathrm{dln}\rho/\mathrm{dln}v_s$	Ref.
S20RTS	**0.5**	0.3	Ritsema et al. (1999)
TX2011	0.5	0.3	Grand (2002)
PRI-05	Inverted for	0.3	Montelli et al. (2006)
HMSL-06	Inverted for	0.3	Houser et al. (2008)
GyPSuM	Inverted for	0.3	Simmons et al. (2010)
SAW642ANb	**0.5**	**0.33**	Panning et al. (2010)
SEMum	**0.5**	**0.3**	Lekić and Romanowicz (2011)
S40RTS	**0.5** (0 km) - **0.33** (2891 km)	**0.5**	Ritsema et al. (2011)
savani	0.5	0.3	Auer et al. (2014)
SEMUCB-WM1	**0.5**	0.3	French and Romanowicz (2014)
S362WMANI+M	**0.55**	0.3	Moulik and Ekström (2014)
SGLOBE-rani	**0.5**	**0.4**	Chang et al. (2014)
SPani	Inverted for	0.3	Tesoniero et al. (2015)
SP12RTS	Inverted for	**0.3**	Koelemeijer et al. (2016)
s10mean	0.5	0.3	Doubrovine et al. (2016)
TX2015	0.5	0.3	Lu and Grand (2016)

Fig. S1 shows isotropic sensitivity kernels for degrees $s = 2, 4, 6, 8$ for the same spheroidal modes as in Figure 1 in the main text. Although the sensitivity to v_s and ρ depends on the spherical harmonic degree, Fig. S1 indicates that kernels for different degrees are not significantly different. Kernels for v_p do not depend on the spherical harmonic degree and are therefore not shown.

In Fig. S2 we show the results for both the upper (top) and lower mantle (bottom) from synthetic tests where we vary how the crust is treated. In the rows titled "CORRECTION", we correct the splitting functions using the crustal thickness from model CRUST5.1 (in addition to surface topography and water level) before performing SOLA inversions. In the rows titled "NOISE", the crustal thickness is not included in the crustal corrections, but instead part of the 3D noise. To do this, we compute the 3D noise arising from crustal thickness uncertainties in a similar way as explained in Section 3.5: we calculate splitting function predictions for just the crustal thickness model (no mantle structure), using either model CRUST5.1 (Mooney et al., 1998), model CRUST2.0 (Laske et al., 2013), or the crustal thickness models developed with SGLOBE-rani (Chang et al., 2015) and SEMUCB-WM1 (French and Romanowicz, 2014). The 3D noise of each mode and each coefficient is approximated by the largest predicted value, which is a conservative estimate. The output maps obtained in both cases look very similar to each other, with differences in amplitudes less than 5%. This justifies our choice to use crustal thickness corrections instead of including it in the noise.

Fig. S3 and S4 show the v_s perturbations obtained from the application of SOLA to the cases DATA-N and RAND-N, respectively. As expected, the uncertainties are significantly lower than we add additional 3D noise (Fig. 4 in the main text), with the relative uncertainty being between 4.7 and 15.5% for DATA-N and between 3.8 and 14.8% for RAND-N. Apart from the reduction in the uncertainties, the use of only data or random noise does not lead to significant differences compared to the map obtained with 3D noise (case 3D-N).

Fig. S5 and S6 show the v_p perturbations obtained from the application of SOLA to the cases DATA-N and RAND-N, respectively. In both cases, the relative uncertainties are always below 13% and the output maps closely resemble the input model both in terms of pattern and amplitudes. When 3D noise is added, this changes significantly and we are not able to recover the pattern and/or the amplitudes of v_p in the first three layers. Moreover, in those layers the relative uncertainties surpass our threshold of 50%. This suggest that the 3D noise (especially from v_s) affects both the model uncertainties and the recovered v_p structure strongly.

Fig. S7 presents our values of R in the four layers that span the whole mantle, estimated by taking the mean of the histograms or from the slope of the best-fitting line. The ratio increases from the surface to the CMB, in agreement with previous studies, although we would not interpret the results in the upper mantle (UM) layer as $\mathrm{dln}v_p$ amplitudes are biased here (see Section 4.4 in the main text).

Fig. S8 presents the geographical variations of R for both our synthetic experiments and real data inversions, for the lowest layer in the mantle. Given the lack of uncertainty information and the low harmonic degree of our model parameterisation ($s = 8$), we refrain from interpreting these maps in terms of *local* variations of R.

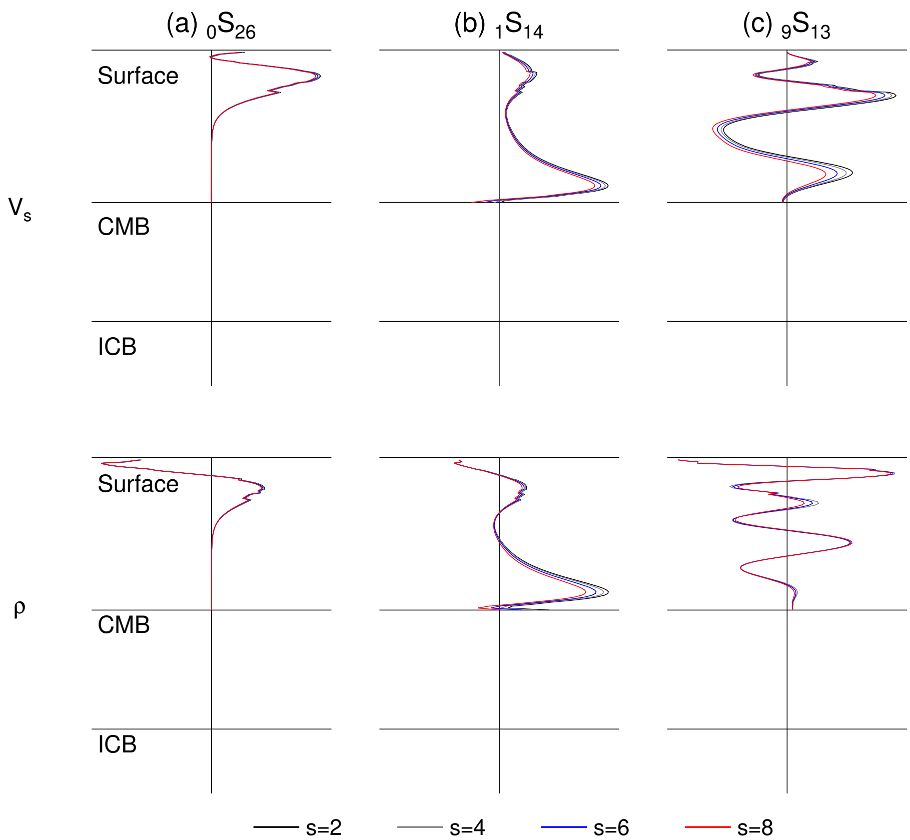

Figure S1: Example sensitivity kernels of spheroidal modes for mantle structure at degrees $s = 2, 4, 6, 8$. We show the sensitivity to shear-wave velocity (top) and density (bottom), calculated for the anisotropic PREM model. Similar to Fig. 1 in the main text.

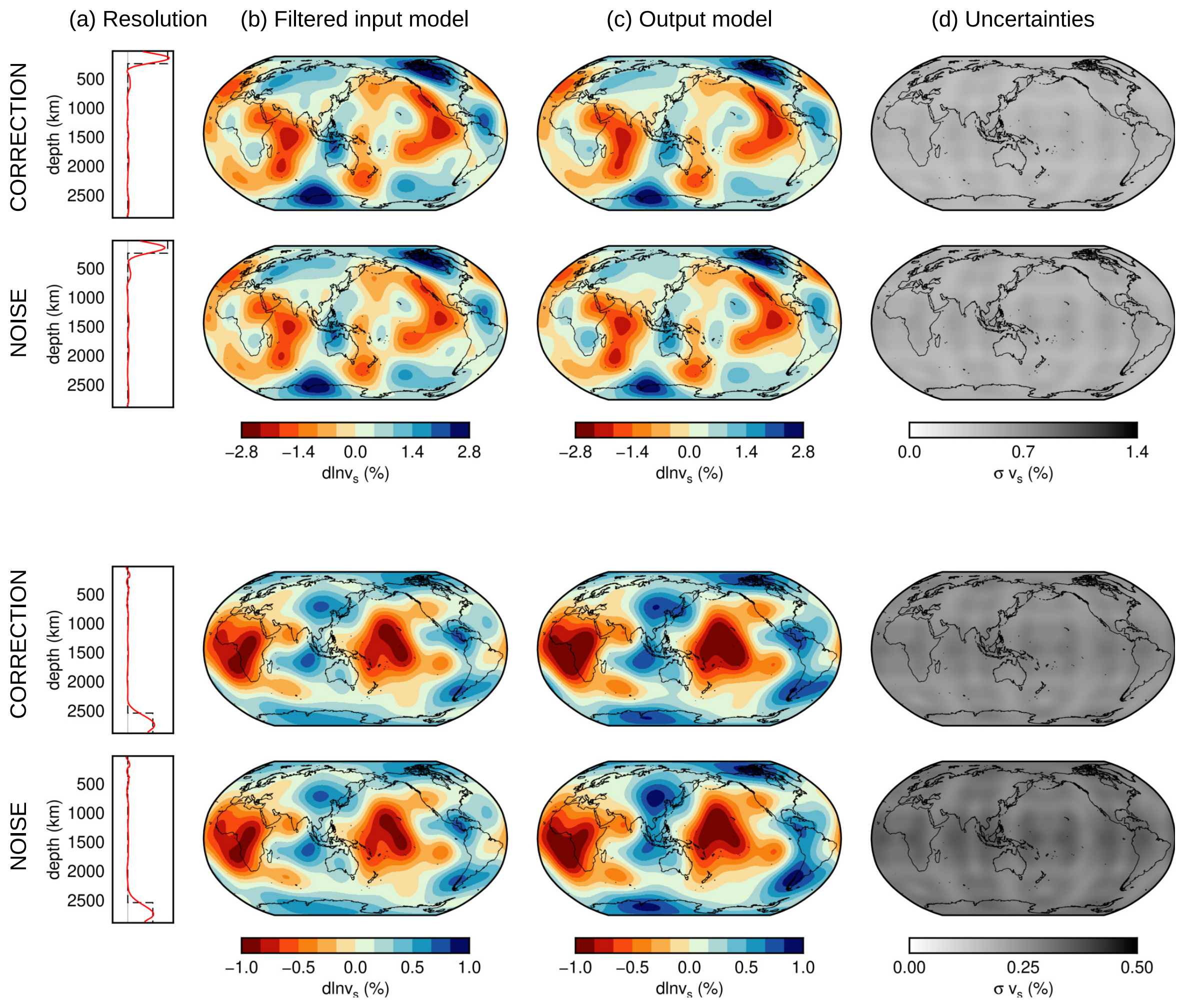

Figure S2: Influence of crustal structure on the synthetic inversion results for v_s perturbations for case 3D-N. For layers in the upper mantle (top) and in the lowermost mantle (bottom), we show: (a) the target and resolving kernels (black and red lines, respectively); (b) the filtered input model; (c) the output model estimate; (d) the output model uncertainties. The crust is either accounted for by crustal corrections (CORRECTION) or included in the 3D noise (NOISE).

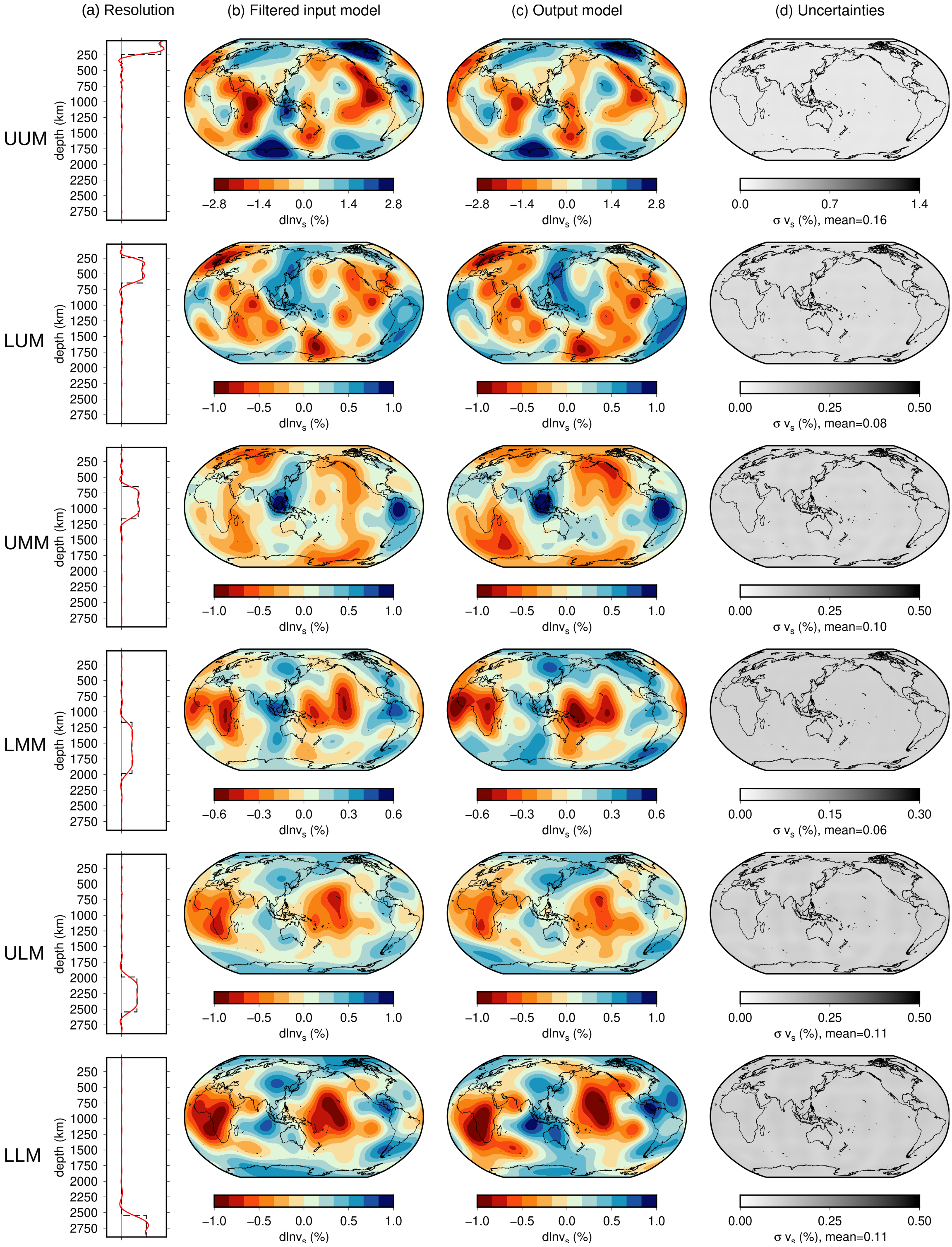

Figure S3: Synthetic inversion results for v_s perturbations with doubled data noise (case DATA-N). Similar to Fig. 4 in the main text.

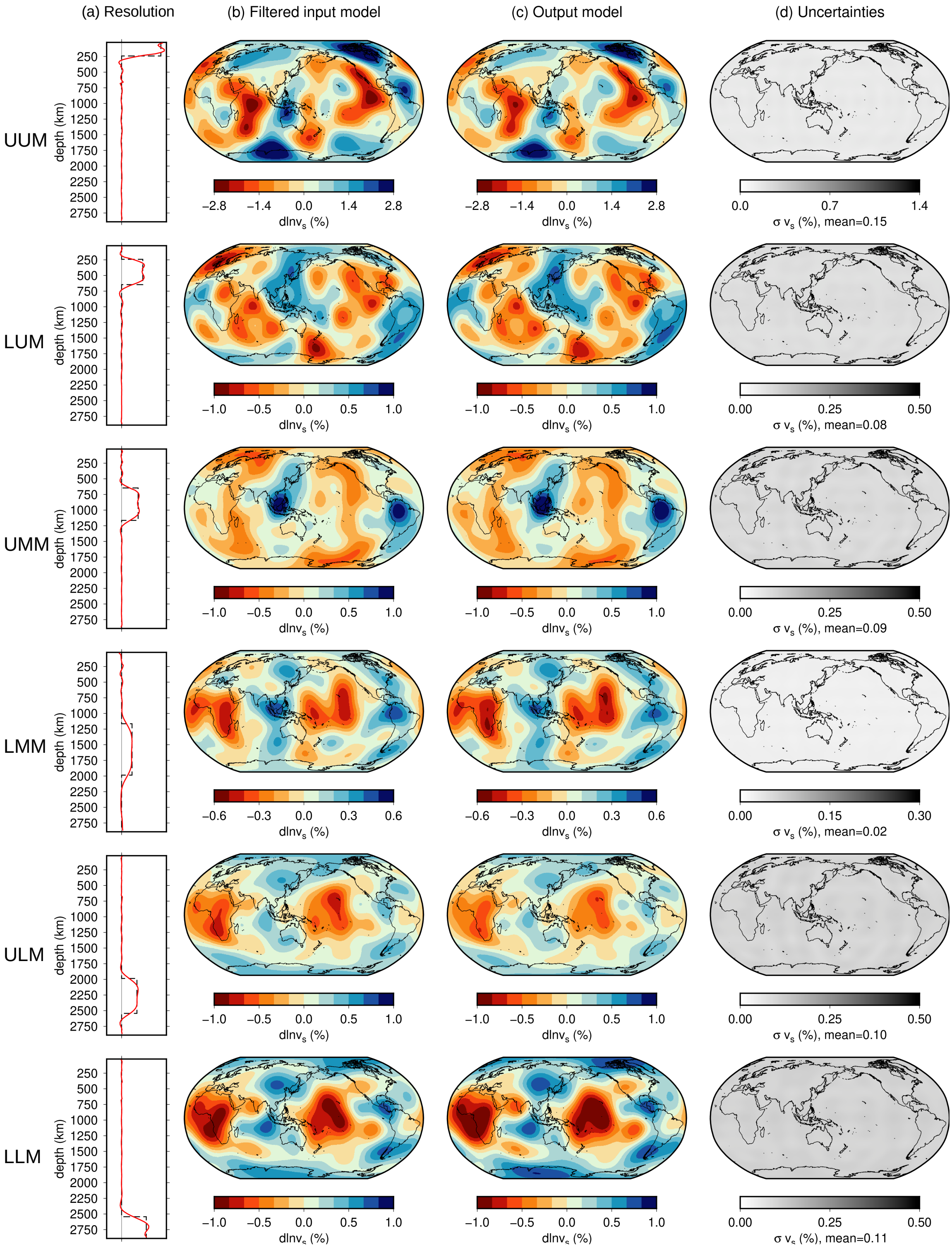

Figure S4: Synthetic inversion results for v_s perturbations with random noise (case RAND-N). Similar to Fig. 4 in the main text.

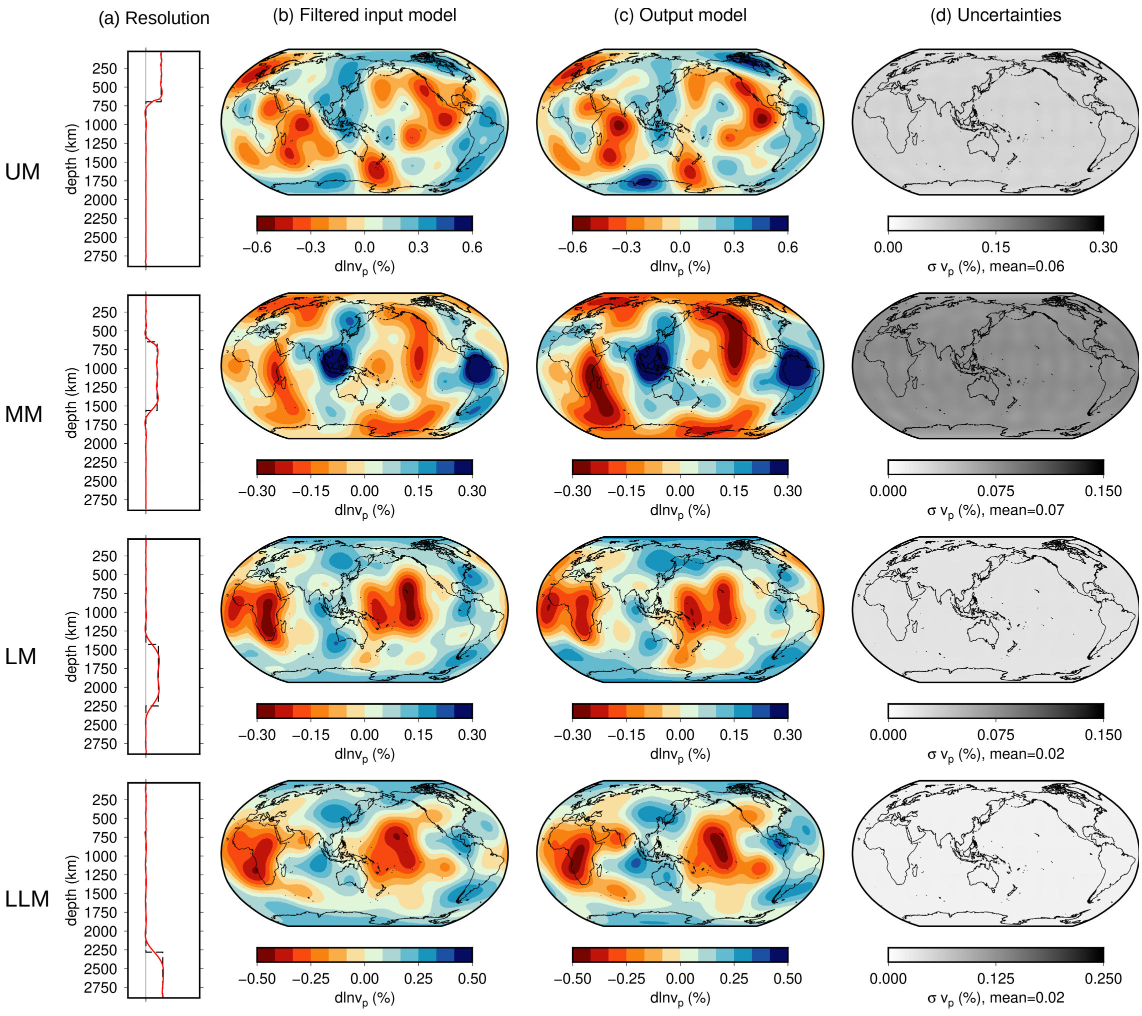

Figure S5: Synthetic inversion results for v_p perturbations with doubled data noise (case DATA-N). Similar to Fig. 5 in the main text.

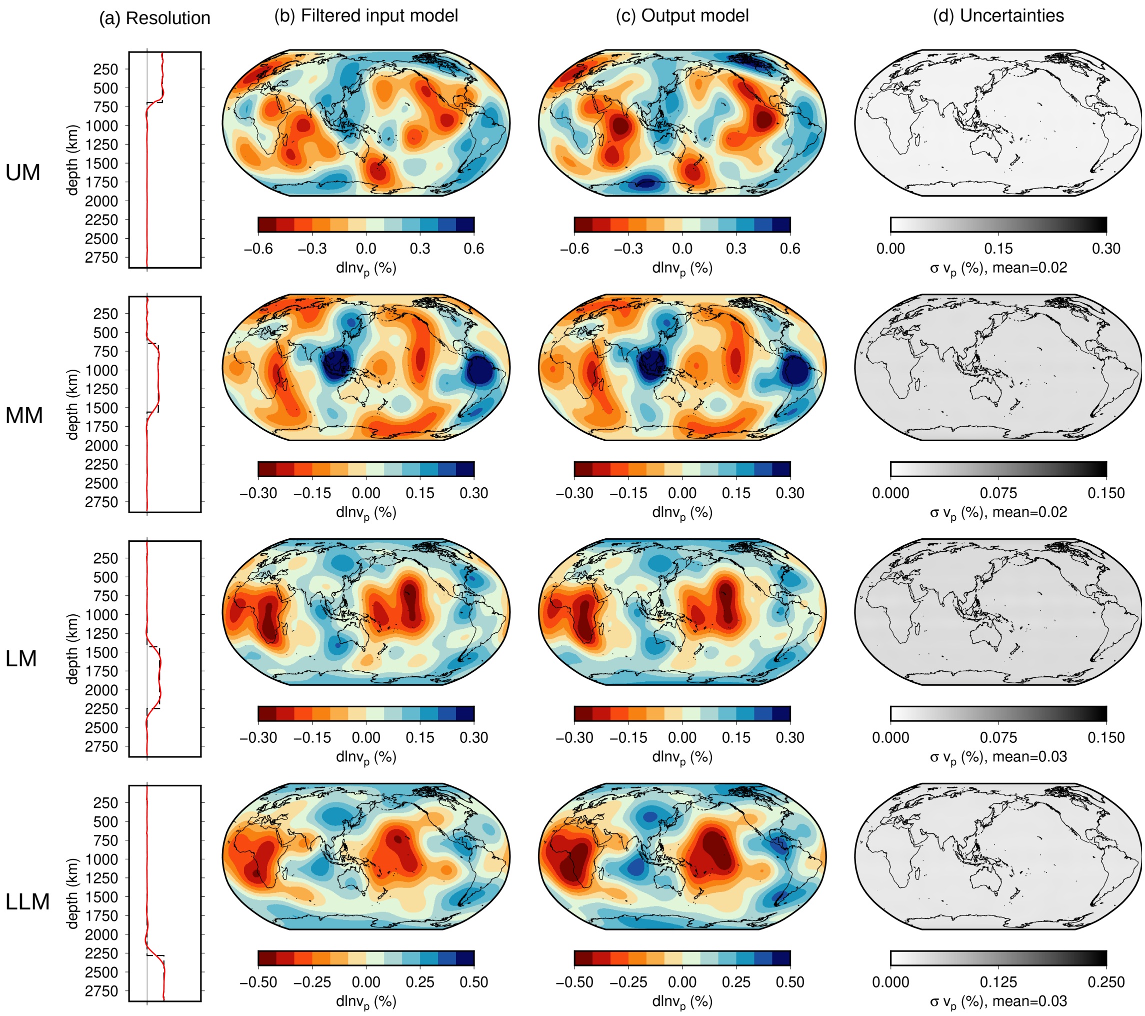

Figure S6: Synthetic inversion results for v_p perturbations with random noise (case RAND-N). Similar to Fig. 5 in the main text.

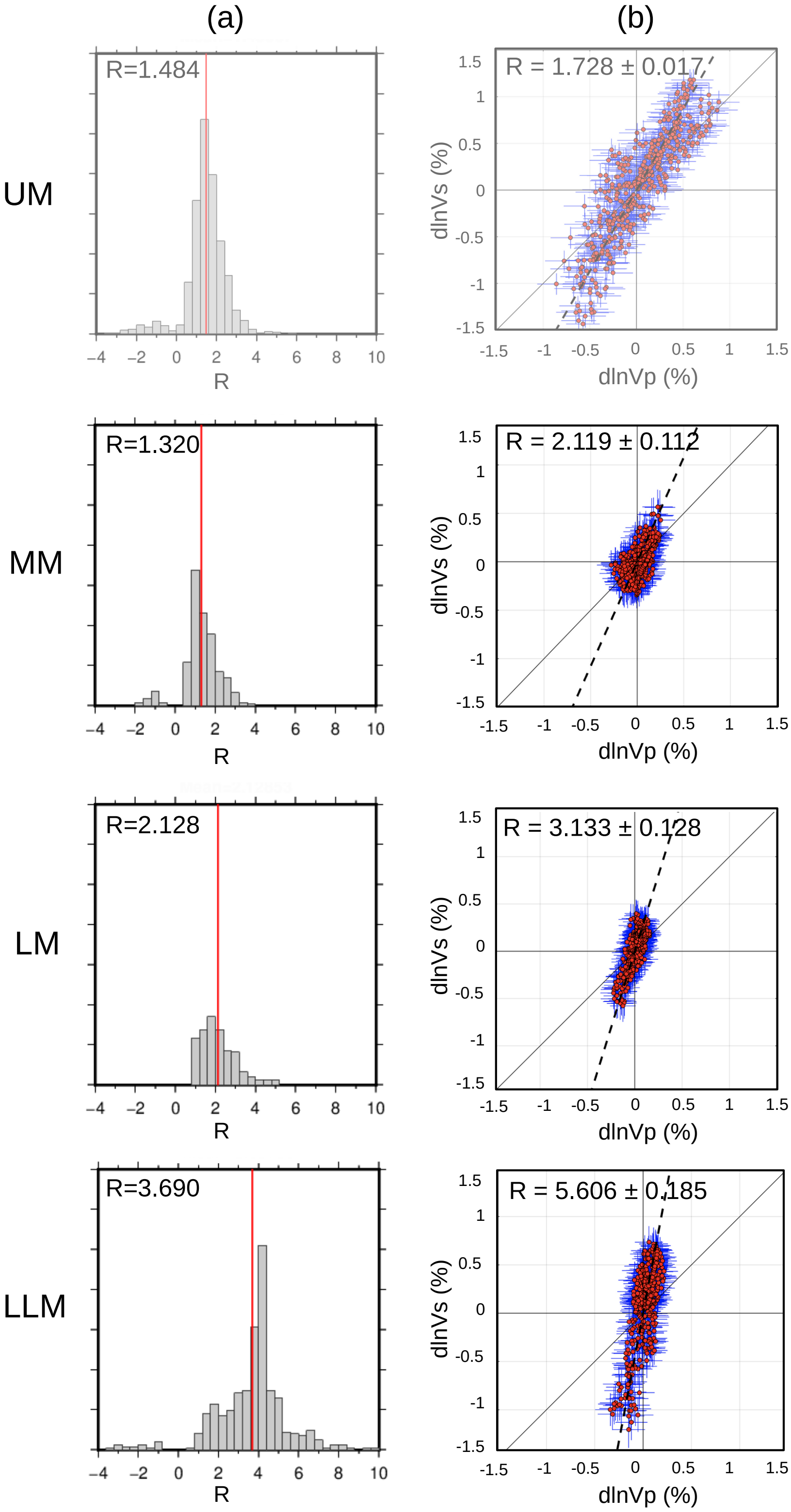

Figure S7: Estimates of the ratio $R = \mathrm{dln}v_s/\mathrm{dln}v_p$ for real data inversions for each of the four layers associated with the resolving kernels in e.g. Fig. 9 in the main text. Here, we illustrate the computation of R as the mean of the histograms resulting from a point-by-point division (a) and as the slope of the best-fitting straight line (b). In panels (b) red circles represent pairs of ($\mathrm{dln}v_p$, $\mathrm{dln}v_s$) for points uniformly located on a sphere, blue lines represent the error bars on both axes. Note that the ratio in the first (upper mantle, UM) layer should not be interpreted given the synthetic test results in Fig. 5 of the main text.

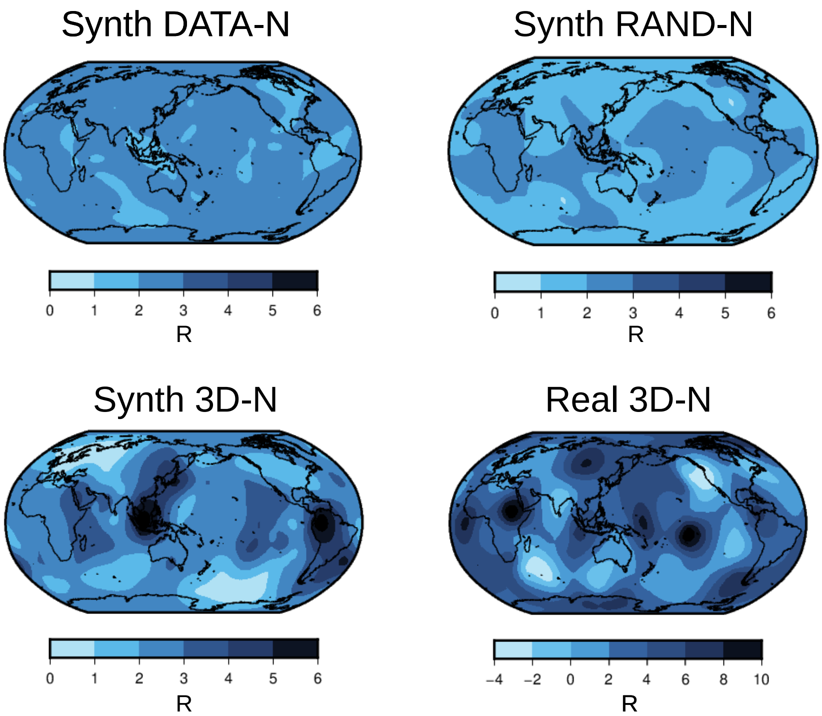

Figure S8: Maps depicting the lateral variations in R, the ratio of dlnv_s and dlnv_p, in the lowest layer in the mantle (i.e. the layer associated with the resolving kernel in Fig. 6 in the main text). The maps are constructed using a point-by-point division of the dlnv_s and dlnv_p maps of Fig. 6 and 10 in the main text. We only include points with $|\mathrm{dln}v_s| > 0.1\%$ and $|\mathrm{dln}v_p| > 0.1\%$.

Bibliography

Auer, L., Boschi, L., Becker, T., Nissen-Meyer, T., and Giardini, D. (2014). Savani: A variable resolution whole-mantle model of anisotropic shear velocity variations based on multiple data sets. *J. Geophys. Res.* , 119(4):3006–3034.

Chang, S.-J., Ferreira, A. M., Ritsema, J., Heijst, H. J., and Woodhouse, J. H. (2015). Joint inversion for global isotropic and radially anisotropic mantle structure including crustal thickness perturbations. *Journal of Geophysical Research: Solid Earth*.

Chang, S.-J., Ferreira, A. M., Ritsema, J., van Heijst, H. J., and Woodhouse, J. H. (2014). Global radially anisotropic mantle structure from multiple datasets: a review, current challenges, and outlook. *Tectonophysics*, 617:1–19.

Doubrovine, P. V., Steinberger, B., and Torsvik, T. H. (2016). A failure to reject: Testing the correlation between large igneous provinces and deep mantle structures with edf statistics. *Geochemistry, Geophysics, Geosystems*, 17(3):1130–1163.

French, S. and Romanowicz, B. (2014). Whole-mantle radially anisotropic shear velocity structure from spectral-element waveform tomography. *Geophys. J. Int.* , 199(3):1303–1327.

Grand, S. P. (2002). Mantle shear–wave tomography and the fate of subducted slabs. *Philosophical Transactions of the Royal Society of London. Series A: Mathematical, Physical and Engineering Sciences*, 360(1800):2475–2491.

Houser, C., Masters, G., Shearer, P., and Laske, G. (2008). Shear and compressional velocity models of the mantle from cluster analysis of long-period waveforms. *Geophys. J. Int.* , 174(1):195–212.

Koelemeijer, P., Ritsema, J., Deuss, A., and Van Heijst, H.-J. (2016). SP12RTS: a degree-12 model of shear-and compressional-wave velocity for Earth's mantle. *Geophys. J. Int.* , 204(2):1024–1039.

Laske, G., Masters, G., Ma, Z., and Pasyanos, M. (2013). Update on crust1. 0—a 1-degree global model of earth's crust. In *Geophys. res. abstr*, volume 15, page 2658.

Lekić, V. and Romanowicz, B. (2011). Inferring upper-mantle structure by full waveform tomography with the spectral element method. *Geophysical Journal International*, 185(2):799–831.

Lu, C. and Grand, S. P. (2016). The effect of subducting slabs in global shear wave tomography. *Geophys. J. Int.* , 205(2):1074–1085.

Montelli, R., Nolet, G., Dahlen, F., and Masters, G. (2006). A catalogue of deep mantle plumes: New results from finite-frequency tomography. *Geochemistry, Geophysics, Geosystems*, 7(11).

Mooney, W., Laske, G., and Masters, T. (1998). CRUST 5.1: A global crustal model at 5×5 °. *J. Geophys. Res.* , 103(B1):727–747.

Moulik, P. and Ekström, G. (2014). An anisotropic shear velocity model of the Earth's mantle using normal modes, body waves, surface waves and long-period waveforms. *Geophys. J. Int.* , 199(3):1713–1738.

Panning, M., Lekić, V., and Romanowicz, B. (2010). Importance of crustal corrections in the development of a new global model of radial anisotropy. *J. Geophys. Res.* , 115(B12).

Ritsema, J., Deuss, A., van Heijst, H.-J., and Woodhouse, J. H. (2011). S40RTS: a degree-40 shear-velocity model for the mantle from new Rayleigh wave dispersion, teleseismic traveltime and normal-mode splitting function measurements. *Geophys. J. Int.* , 184(3):1223–1236.

Ritsema, J., van Heijst, H.-J., and Woodhouse, J. (1999). Complex shear wave velocity structure imaged beneath Africa and Iceland. *Science* , 286(5446):1925.

Simmons, N. A., Forte, A. M., Boschi, L., and Grand, S. P. (2010). GyPSuM: A joint tomographic model of mantle density and seismic wave speeds. *J. Geophys. Res.* , 115(B12).

Tesoniero, A., Auer, L., Boschi, L., and Cammarano, F. (2015). Hydration of marginal basins and compositional variations within the continental lithospheric mantle inferred from a new global model of shear and compressional velocity. *J. Geophys. Res.* , 120(11):7789–7813.